THE PENNSYLVANIA STATE UNIVERSITY
SCHREYER HONORS COLLEGE

DEPARTMENT OF AEROSPACE ENGINEERING

AMENDMENT TO GLAUERT'S OPTIMUM ROTOR DISK SOLUTION

DIVYA TYAGI
SPRING 2024

A thesis
submitted in partial fulfillment
of the requirements
for a baccalaureate degree
in Aerospace Engineering
with honors in Aerospace Engineering

Reviewed and approved* by the following:

Sven Schmitz
Boeing/A. D. Welliver Professor of Aerospace Engineering
Thesis Supervisor

Namiko Yamamoto
Associate Professor of Aerospace Engineering
Honors Adviser

*Signatures are on file in the Schreyer Honors College.

Abstract

Glauert's rotor disk theory serves as the basis for wind turbine aerodynamics research, guiding the design and development of optimum rotors. The long-established objective function in turbine optimization is the maximization of power extraction from the wind. This thesis is an amendment to Glauert's original work on the optimum rotor disk solution, and it consists of analytical derivations for power, thrust, and bending moment coefficients (C_P, C_T, C_{Be}). Additionally, an alternate mathematical approach is taken towards the optimization problem by means of calculus of variations. Glauert's original distributions for axial and angular induction factors (a and a') are recovered through the course of this amended work. Also included in this amendment are derivations for the exact integrals defining the thrust and bending moment coefficients as functions of tip speed ratio (λ). An interesting finding pertaining to the convergence behavior for such coefficients is revealed—the thrust and bending moment coefficients have a finite, non-zero value as the tip speed ratio approaches 0, which is proven analytically using L'Hôpital's theorem. Indeed, the limiting case for the thrust and bending moment coefficients of the actuator disk are 0.75 and 0.50, respectively.

Table of Contents

List of Figures iv

List of Tables v

Nomenclature vi

Acknowledgements vii

1 Introduction 1
- 1.1 Overview . . . 2
- 1.2 History of Wind Turbines . . . 2
- 1.3 Thesis Outline . . . 4
- 1.4 Basics of Momentum Theory . . . 4
  - 1.4.1 Actuator Disk Theory . . . 4
  - 1.4.2 Rotor Disk Theory . . . 6
  - 1.4.3 Non-Dimensional Induction Factors . . . 7

2 Optimum Wind Turbine Rotor Performance Accounting for Wake Rotation 9
- 2.1 Glauert's Optimum Solution . . . 10
  - 2.1.1 Limiting Case for Low and High Tip Speed Ratio . . . 12
  - 2.1.2 Derivation of Maximum Power Coefficient . . . 13
- 2.2 Optimum Wind Turbine Rotor Models in Literature . . . 16

3 Amendment to Glauert's Optimum Rotor Model 19
- 3.1 Derivation of Thrust Coefficient Based on Glauert's Optimum Solution . . . 20
- 3.2 Derivation of Bending Moment Coefficient Based on Glauert's Optimum Solution . 23
- 3.3 Summary of Coefficients Derived from Glauert's Optimum Model . . . 26
- 3.4 A Calculus of Variations Approach to Glauert's Optimum Solution . . . 28
  - 3.4.1 Glauert's Optimum Rotor Model with Original Pressure Balance . . . 28
  - 3.4.2 Establishing a Relation for the Optimal Axial Induction Factor $a(\lambda_r)$ . . . 29
  - 3.4.3 Establishing a Relation for the Optimal Angular Induction Factor $a'(\lambda_r)$ . . 30
- 3.5 Optimum Rotor Model of Burton, Sharpe et al. Using Modified Pressure Balance . 30
  - 3.5.1 Modified Relation for Optimal Axial Induction Factor $a(\lambda_r)$ . . . 31
  - 3.5.2 Modified Relation for Optimal Angular Induction Factor $a'(\lambda_r)$ . . . 31
- 3.6 Visual Representation of Flow Conditions Using Different Optimum Models . . . 32

4 Conclusion and Future Work **37**
4.1 Conclusion 38
4.2 Future Work 39

Bibliography **40**

List of Figures

1.1 Blyth's wind turbine powering his holiday home in Marykirk, Scotland in 1891. . . 2
1.2 Educationalist la Cour in front of his experimental turbines in 1899 [1]. 3
1.3 The evolution of wind turbine blade diameters over the last few decades [2]. 4
1.4 Energy extracting axi-symmetric streamtube of a wind turbine. 5
1.5 Wind speed distribution inside axi-symmetric streamtube of a wind turbine. 6
1.6 Energy extracting axi-symmetric streamtube of a wind turbine including wake rotation. 7

2.1 Glauert's theoretical solutions for optimum axial and angular induction factors, a and a' respectively, as a function of local tip speed ratio, λ_r 12
2.2 Maximum power coefficient, C_{Pmax}, for Glauert's actuator disk model and Betz's theoretical limit. 16

3.1 Thrust coefficient C_T as a function of tip speed ratio, λ. for optimal a and a' distribution. 22
3.2 Bending moment coefficient C_{Be} as a function of tip speed ratio, λ. for optimal a and a' distribution. 26
3.3 Power C_P, thrust C_T, and bending moment coefficients C_{Be} as functions of tip speed ratio, λ. for optimal a and a' distribution. 27
3.4 Spanwise derivatives of power, thrust, and bending moment coefficients per unit length as a function of the non-dimensional blade radius, $\frac{r}{R}$, for a range of design tip speed ratios. 28
3.5 Comparison of optimum flow distributions for Glauert's solution, the amendment, and the optimum model of Burton and Sharpe using universal solution (left) and scaled spanwise distributions (right) for $\lambda = 4$ (black) and $\lambda = 8$ (red). 33
3.6 Power coefficient C_P variation between Glauert's model and the amended model for local tip speed ratios, λ_r. 34
3.7 Thrust coefficient C_T variation between Glauert's model and the amended model for low tip speed ratios, λ_r. 35
3.8 Bending moment coefficient C_{Be} variation between Glauert's model and the amended model for low tip speed ratios, λ_r. 36

List of Tables

2.1 Optimum induction factors for Glauert's actuator disk model. 12
2.2 Maximum power coefficient, C_{Pmax}, for Glauert's actuator disk model. 16

3.1 Thrust coefficient, C_T, for Glauert's actuator disk model. 22
3.2 Bending moment coefficient, C_{Be}, for Glauert's actuator disk model. 26
3.3 Variation in maximum power coefficient between Glauert's actuator disk model ($C_{Pmax,G}$) and the amended model ($C_{Pmax,A}$). 33
3.4 Variation in thrust coefficient, C_T, between Glauert's actuator disk model and the amended model. 34
3.5 Variation in bending moment coefficient, C_{Be}, between Glauert's actuator disk model and the amended model. 35

Nomenclature

λ	Tip speed ratio
$\mathcal{L}$	Lagrangian
Ω	Angular speed
ω	Wake angular velocity
ρ	Density
A	Area
a	Axial induction factor
a'	Angular induction factor
Be	Bending moment
C_P	Power coefficient
C_T	Thrust coefficient
C_{Be}	Bending moment coefficient
m	Mass
P	Power
p	Pressure
R	Blade radius
r	Spanwise blade station
T	Thrust
V	Velocity

Acknowledgements

I would like to express the sincerest gratitude towards my adviser, Dr. Sven Schmitz, for always going above and beyond to support my personal and professional development. His intellectual guidance and patience towards my research efforts is a large contributor to the successful completion of my undergraduate honors thesis. Also, thank you to my honors adviser, Dr. Yamamoto, for reviewing this thesis.

Additionally, I would like to extend my thanks to graduate student, Desirae Major, who took me under her wing and introduced me to wind energy. I would also like to extend my appreciation towards our current research group, Pierce Hart, Sam Johnson, AJ Abraham, and Maryam Farhat, for all of the good times and constant laughter in the lab.

Last but not least, I would like to express my thanks to family and friends for their words of encouragement during the thesis writing process.

I wish to dedicate this undergraduate thesis to my dad, in loving memory.

Chapter 1

Introduction

1.1 Overview

The transition towards clean energy sources has gained significant traction globally, with wind energy being a primary contributor to sustainable energy generation void of carbon emissions. Just in the United States, wind power is the fourth-largest source of electricity generation, carrying the ability to provide clean, cost-competitive power to over 46 million American homes [3]. The Intergovernmental Panel on Climate Change (IPCC) recognizes that wind energy is a publicly favored climate change mitigation effort that has become increasingly cost effective, and therefore supports its deployment globally [4]. Goal 7 under the 2030 Agenda for Sustainable Development adopted by the United Nations General Assembly calls for access to affordable, reliable, sustainable, and modern energy amongst society as a whole [5]. Ongoing investments into wind turbine development and optimization efforts are imperative in order to keep the commitment to minimizing anthropogenic, or human inflicted, climate change. The functionality of wind turbines can be studied using foundational aerodynamic principles, which of course are coupled with experimental and computational methods in wind energy research today.

1.2 History of Wind Turbines

Up until the late nineteenth century, windmills were primarily used as mechanical power sources for purposes such as sawing wood, grinding grain, and lifting water from wells. James Blyth of Scotland contributed to the development of modern vertical and horizontal-axis wind turbines in 1887, fusing together the windmill with an electric generator to create a "wind engine." His wind turbine consisted of a tripod design, supporting 4 meter blades carrying canvas sails. Shortly after Blyth's contributions to wind turbine technology, American innovator Charles Brush decided to build the first turbine North America had seen at 18 meters tall with blade lengths exceeding 17 meters [6].

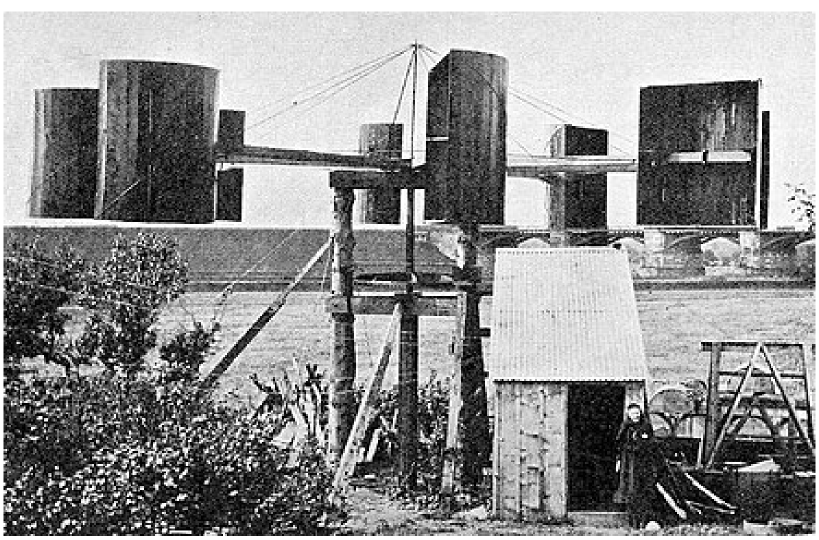

Figure 1.1: Blyth's wind turbine powering his holiday home in Marykirk, Scotland in 1891.

In 1891, European inventor Poul la Cour was responsible for building the first wind turbine in

Denmark. La Cour undertook years of blade research through wind tunnel testing, and La Cour was able to prove the direct relationships between power, wind speed, and swept blade area. His work had a lasting impact on Denmarks' electricity generation capabilities, as by 1910, the nation had over 100 wind turbines in operation for agricultural use [6].

Figure 1.2: Educationalist la Cour in front of his experimental turbines in 1899 [1].

Throughout the 20th century, there continued to be stable wind turbine developments across the globe. Some notable structures were the 100 kW Balaclava wind turbine of 1931, the Smith-Putnam first 1 MW turbine of 1941, the 200 kW Gedser turbine of 1956, as well as the 1.1 MW Electricité de France turbine of 1963. It was not until the exponential rise of oil prices in the early 1970's that wind energy production experienced a steep interest by investors [7].

There have been trends in wind turbine development to produce bigger wind turbines—in terms of both hub height and blade diameter. In regard to hub height, taller turbine towers have the ability to capture greater amounts of energy, as increased altitudes generally result in increased winds. It is projected that the average hub height for offshore wind turbines in the United States will reach 150 meters by 2035 [8].

The relationship between power generated by a turbine and its rotor diameter is as follows: $P \propto D^2$. As expected, future turbine design aims for larger rotor diameters in order for the blades to sweep more area, hence producing more electricity. According to experts, it is anticipated that rotor diameters will face rapid growth—at 174 meters for onshore turbines and 250 meters for offshore turbines [9]. Figure 1.3 captures the growth of rotor diameters from the operational year of 1990 to 2015. As observed, in just 25 years, wind turbine blade diameters have grown by approximately 263%.

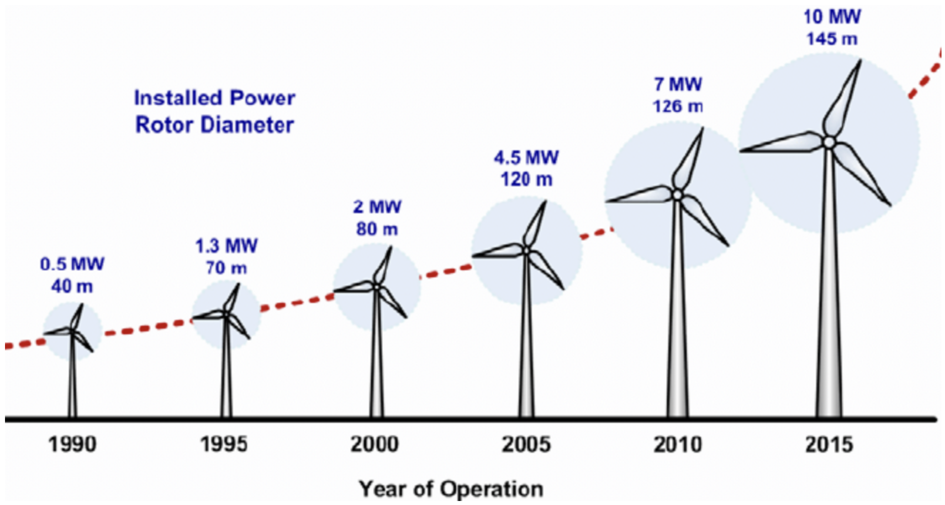

Figure 1.3: The evolution of wind turbine blade diameters over the last few decades [2].

1.3 Thesis Outline

This undergraduate thesis is structured into 4 chapters. Chapter 1 gives a high-level overview on wind energy—touching on global sustainability initiatives, the history of wind turbines, and a fundamental aerodynamics review. Chapter 2 discusses different wind turbine aerodynamic models capturing optimum performance, while delving further into Glauert's rotor disk theory. Chapter 3 serves as an amendment to Glauert's work, presenting an analytical derivation for the exact thrust and bending moment coefficients associated with Glauert's optimum model. Additionally, this chapter includes an alternate mathematical approach to recover Glauert's optimum induction factor distributions by means of calculus of variation. The optimization problem is taken one step further to account for the complete integrand within the definition of power coefficient, and those results are then compared to Glauert's existing model. Finally, Chapter 4 concludes this thesis work and proposes next steps. This work has also been submitted to the AIAA Regional Student Conference.

1.4 Basics of Momentum Theory

As a brief introduction, momentum theory allows for simplifications to be applied to the complex systems of wind turbines with the ultimate goal of better understanding operating conditions in time-varying, three dimensional, and turbulent flow conditions [10]. This theory is built on framework set by the actuator disk model, and is reformulated within the rotor disk model to account for angular momentum and kinetic energy added from wake rotation [11].

1.4.1 Actuator Disk Theory

A classical method of analyzing wind turbines is through a streamtube representation. Consider an axi-symmetric streamtube which encompasses a wind turbine, as well as the axial wind passing through it, as portrayed in Fig. 1.4. The cross section at the rotor is modeled as the actuator disk.

The actuator disk is a circular, infinitely thin area inside which the turbine's blades rotate. As a reference, section 1 represents the entrance of the streamtube, section 2 represents the actuator disk, and section 3 represents the exit plane of the streamtube.

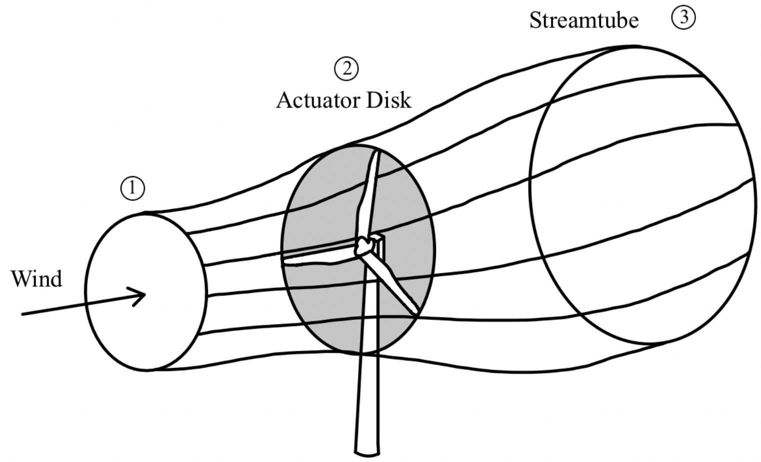

Figure 1.4: Energy extracting axi-symmetric streamtube of a wind turbine.

Within the streamtube, mass, momentum, and energy flux are conserved. The uniform, one-dimensional velocity that initially enters the streamtube is slowly extracted in the form of momentum and energy by the turbine; as a result, velocity decreases past the actuator disk and the streamtube area increases as a consequence of mass conservation. Therefore, the mass flow rate, $\dot{m}$, is equal along the entire streamtube, including at the entrance, actuator disk, and exit plane as depicted by Eq. (1.1).

$$\dot{m}_1 = \dot{m}_2 = \dot{m}_3 \tag{1.1}$$

See Fig. 1.5 for a cross-sectional view of the streamtube. The mass flow rate can be defined by the fluid density ρ, velocity V, and actuator disk area A, as shown in Eq. (1.2). With the assumption of incompressible flow under the actuator disk model, note that the fluid density is constant throughout the streamtube.

$$\rho V_1 A_1 = \rho V_2 A_2 = \rho V_3 A_3 \tag{1.2}$$

There exists a pressure jump, Δp, across the actuator disk area, A, which causes a thrust force, T in the streamwise direction. This external force on the streamtube is exactly balanced by the axial momentum of the control volume, as equated in Eq. (1.3).

$$T = \Delta p A = \dot{m}(V_1 - V_3) \tag{1.3}$$

Substituting the mass flow rate relation for $\dot{m}$ yields the following relationship present in Eq. (1.4).

$$\Delta p A = \rho V_2 A (V_1 - V_3) \tag{1.4}$$

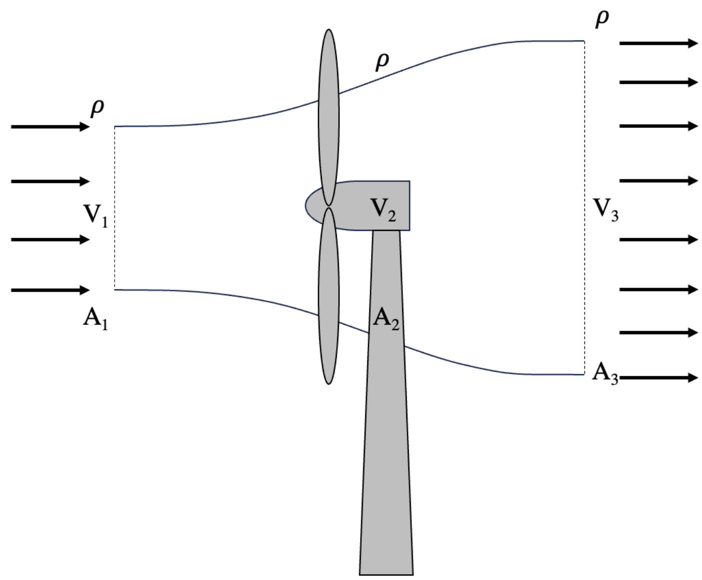

Figure 1.5: Wind speed distribution inside axi-symmetric streamtube of a wind turbine.

To define the pressure jump present at the actuator disk in terms of V_1 and V_3, Bernoulli's principle must be applied. Since there exists a discontinuity in pressure at the actuator disk, Bernoulli's equation must be applied both upstream and downstream of the actuator disk. See Eq. (1.5) for the upstream application, and see Eq. (1.6) for the downstream application.

$$p_0 + \frac{1}{2}\rho V_1^2 = p + \frac{1}{2}\rho V_2^2 \tag{1.5}$$

$$(p - \Delta p) + \frac{1}{2}\rho V_2^2 = p_0 + \frac{1}{2}\rho V_3^2 \tag{1.6}$$

Subtracting Eq. (1.5) by Eq. (1.6) yields a more simplified expression for the pressure jump present at the actuator disk, as depicted by Eq. (1.7) [10].

$$\Delta p = \frac{1}{2}\rho(V_1^2 - V_3^2) \tag{1.7}$$

1.4.2 Rotor Disk Theory

Now, there is an added dimension to the previous streamtube analysis—wake rotation—as depicted in Fig. 1.6. A rotor disk model is introduced, accounting for wake rotation resulting from the angular momentum and kinetic energy of the rotating disk at an angular speed, Ω. The wake angular velocity component, ω, results from rotor torque in the circumferential direction. It impacts the overall efficiency of the turbine, thus also causing a decrease in the maximum attainable power coefficient. The assumptions of the rotor disk model are as follows: one-dimensional, steady, incompressible, inviscid and irrotational flow.

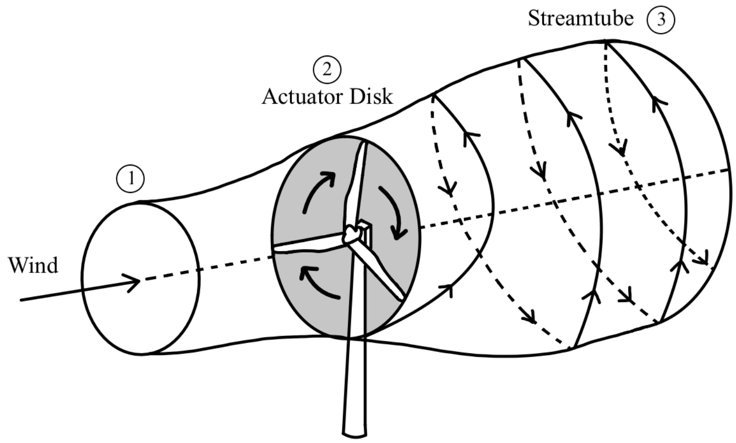

Figure 1.6: Energy extracting axi-symmetric streamtube of a wind turbine including wake rotation.

Now, the wake rotation must be integrated to accurately portray the pressure jump across the rotor disk. In this case, the energy relation should be applied both upstream and downstream of the rotor disk with the assumption that Δp is solely used to generate power.

The upstream energy equation is as follows in Eq. (1.8). Again, Ω is the rotor disk's angular speed and r is the radial location of the disk's annulus.

$$p + \frac{1}{2}\rho(\Omega r)^2 \tag{1.8}$$

The downstream energy equation is presented in Eq. (1.9).

$$(p - \Delta p) + \frac{1}{2}\rho[(\Omega + \omega)r]^2 \tag{1.9}$$

Setting the two equations from above equal to each other results in a new Δp equation representative of rotor disk theory, as shown in Eq. (1.10) [10].

$$\Delta p = \rho(\Omega + \frac{1}{2}\omega)\omega r^2 = 2\rho(1 + \frac{\omega}{2\Omega})\frac{\omega}{2\Omega}\Omega^2 r^2 \tag{1.10}$$

These relations for the pressure jump based on momentum theory will return in the subsequent section, serving as useful groundwork for the rest of this thesis.

1.4.3 Non-Dimensional Induction Factors

It is common practice to use non-dimensional coefficients in engineering analysis, allowing for various test cases to be compared at once. In wind turbine aerodynamics, there are two essential non-dimensional coefficients which define the axial velocity and wake rotation, respectively. The axial induction factor, a, can be used to represent the reduction in wind speed at the actuator disk in comparison to the freestream velocity. This dimensionless coefficient is defined in Eq. (1.11), where V_1 is the wind speed at the entrance plane and V_2 is the speed at the rotor disk.

$$a = 1 - \frac{V_2}{V_1} \tag{1.11}$$

The angular induction factor, a', relates the wake angular velocity component to its angular speed, as shown in Eq. (1.12) [10].

$$a' = \frac{\omega}{2\Omega} \tag{1.12}$$

Equation (1.7) is rewritten in terms of the axial induction factor, a, below in Eq. (1.13).

$$\Delta p = 2\rho V_0^2 a(1-a) \tag{1.13}$$

Similarly, Eq. (1.10) is rewritten in terms of both a and a' as shown in Eq. (1.14).

$$\Delta p = 2\rho V_0^2 a'(1+a')\lambda_r^2 \tag{1.14}$$

With momentum theory applied, a relation between both induction factors can be represented by Eq. (1.15). For future reference, this equation will be referred to as the '1st Relation.'

$$\lambda_r^2 = \frac{a(1-a)}{a'(1+a')} \tag{1.15}$$

Chapter 2

Optimum Wind Turbine Rotor Performance Accounting for Wake Rotation

2.1 Glauert's Optimum Solution

Rotor power, P, is a function of fluid density, freestream velocity, disk area, and the dimensionless power coefficient, C_P as shown in Eq. (2.1).

$$P = \frac{1}{2}\rho V_0^3 A C_P \tag{2.1}$$

Through rotor disk theory, an exact equation for C_P is determined in terms of tip speed ratio, axial and angular induction factors, as shown in Eq. (2.2). Betz's law, computed by physicist Albert Betz, revealed that the maximum power available to be extracted from the wind was $\frac{16}{27}$, or approximately 59.3% [12]; this is the limit case for high λ's in Eq. (2.2).

$$C_P = \frac{8}{\lambda^2}\int_0^{\lambda} a'(1-a)\lambda_r^3 \, d\lambda_r \tag{2.2}$$

In 1935, aerodynamicist Hermann Glauert approached the optimization problem of maximizing C_P using the objective function f as defined in Eq. (2.3). Glauert's decision to focus on this truncated form of f, rather than the complete term of $a'(1-a)\lambda_r^3$ within Eq. (2.2), stems from his belief that the disk annuli operate independently from one another—even though $a'(1-a)$ is incomplete according to the definition of C_P [13].

This expression of interest has been defined by the function f in Eq. (2.3). In order to determine the function's maximum, one must differentiate both sides of the equation with respect to the axial induction factor, a. Equation (2.4) must be set equal to 0 in order to find the appropriate stationary point.

$$f = a'(1-a) \tag{2.3}$$

$$\frac{df}{da} = \frac{da'}{da}(1-a) - a' = 0 \tag{2.4}$$

Simplifying the equation above yields Eq. (2.5), a condition which must be satisfied at maximum C_P.

$$\frac{da'}{da} = \frac{a'}{1-a} \tag{2.5}$$

Returning back to the '1st Relation' presented in Eq. (1.15), a derivative with respect to a is taken on both left and right sides of the equation, yielding Eq. (2.6).

$$1 - 2a = \lambda_r^2(1+2a')\frac{da'}{da} \tag{2.6}$$

For the λ_r^2 term, Eq. (1.15) is substituted in, and for the differential term, Eq. (2.5) is substituted in.

$$\frac{1+a'}{1+2a'} = \frac{a}{1-2a} \tag{2.7}$$

The result of some algebraic rearranging is the '2nd Relation', which has been shown in Eq. (2.8).

$$a' = \frac{1-3a}{4a-1} \tag{2.8}$$

In this relation, the angular induction factor, a', is defined by solely the axial induction factor. Therefore, the solution for a' can be substituted back into the '1st Relation' to yield a relationship between λ_r and a:

$$\lambda_r^2 = \frac{(1-a)(1-4a)^2}{1-3a} \tag{2.9}$$

Equation (2.9) can be rearranged into a third-degree polynomial representing the optimal axial induction factors across the rotor disk as a function of local tip speed ratios.

$$16a^3 - 24a^2 + (9-3\lambda_r^2)a + (\lambda_r^2 - 1) = 0 \tag{2.10}$$

Using the Newton–Raphson algorithm, displayed in Eq. (2.11), a solution for the optimum axial induction factor, a, can be determined for a range of λ_r values.

$$a_{i+1} = a_i - \frac{f(a_i)}{f'(a_i)} \tag{2.11}$$

To begin using this root-finding method, an initial guess is set based on the operating range of a $\in [\frac{1}{4}, \frac{1}{3}]$: $a_0 = 0.3$. From here, Eq. (2.12), which has the appropriate expressions for $f(a_i)$ and $f'(a_i)$ substituted in, is solved iteratively until the convergence criterion set by Eq. (2.13) is met.

$$a_{i+1} = a_i - \frac{16a_i^3 - 24a_i^2 + (9-3\lambda_r^2)a_i + (\lambda_r^2 - 1)}{48a_i^2 - 48a_i + (9-3\lambda_r^2)} \tag{2.12}$$

$$|a_{i+1} - a_i| < 10^{-6} \tag{2.13}$$

Once the values for a have been populated, Eq. (2.8) is used to calculate the angular induction factor, a', for a range of local tip speed ratios. These optimum induction factors have been tabulated in Table 2.1, as well as plotted in Fig. 2.1 for a λ_r range of 0 to 10. As noted in the figure's legend, a is represented by the solid black line and a' is represented by the dashed black line.

Table 2.1: Optimum induction factors for Glauert's actuator disk model.

λ_r	a	a'
0	0.250000	∞
1	0.316987	0.183013
2	0.327896	0.052354
3	0.330747	0.024018
4	0.331842	0.013671
5	0.332367	0.008799
6	0.332658	0.006129
7	0.332835	0.004511
8	0.332951	0.003458
9	0.333031	0.002735
10	0.333088	0.002216

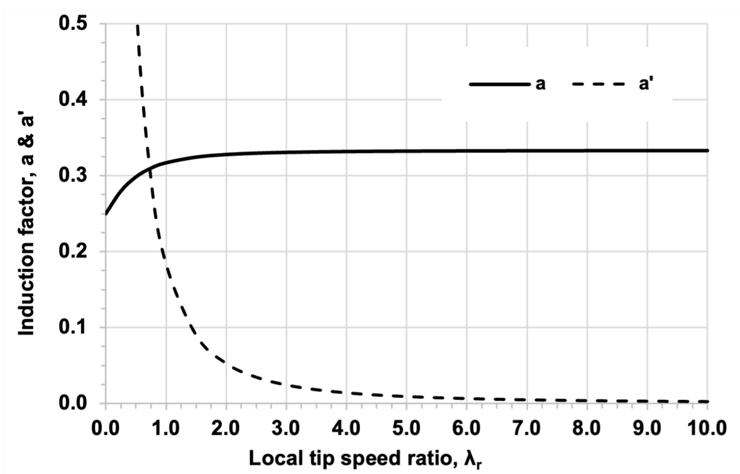

Figure 2.1: Glauert's theoretical solutions for optimum axial and angular induction factors, a and a' respectively, as a function of local tip speed ratio, λ_r

2.1.1 Limiting Case for Low and High Tip Speed Ratio

Once again, the universal relation is written out in Eq. (2.14). The goal now is to understand the behavior of a as λ_r tends to both 0 and infinity.

$$16a^3 - 24a^2 + (9 - 3\lambda_r^2)a + (\lambda_r^2 - 1) = 0 \tag{2.14}$$

First, the lower limiting case of $\lambda_r \to 0$ will be addressed. See Eq. (2.15) for the resulting expression.

$$16a^3 - 24a^2 + 9a - 1 = 0 \tag{2.15}$$

The expression above can be factored into two terms as displayed in Eq. (2.16), from which the zeros can be easily extracted.

$$(a-1)(4a-1)^2 = 0 \tag{2.16}$$

The roots of Eq. (2.16) are $a = \frac{1}{4}$ and 1, and from momentum theory it is known that the valid operating range is $a \in [\frac{1}{4}, \frac{1}{3}]$. Therefore, as λ_r tends to 0, $a = \frac{1}{4}$. Now, the upper limiting case for the universal relation will be handled.

The variables a and λ_r are currently coupled in the equation above. To decouple them, the terms $(1-3a)$ and $(1+\lambda_r^2)$ are factored out through algebraic manipulation, as shown in Eq. (2.17).

$$16a^3 - 24a^2 + 12a - 2 + (1-3a)(1+\lambda_r^2) = 0 \tag{2.17}$$

Next, all of the terms with a are simply kept on the left-hand side of the equation, whereas the term with λ_r^2 is brought to the right-hand side as done so in Eq. (2.18).

$$\frac{16a^3 - 24a^2 + 12a - 2}{1-3a} = -(1+\lambda_r^2) \tag{2.18}$$

Further simplification is done on the equation above, while bringing the $(1+\lambda_r^2)$ term into the denominator, as shown in Eq. (2.19).

$$\frac{1}{1+\lambda_r^2} = \frac{1-3a}{-2(2a-1)^3} \tag{2.19}$$

Now, the limit of the left-hand side of Eq. (2.19) can be taken as $\lambda_r \to \infty$. Since the term in the denominator consists of λ_r^2, this limit approaches 0 as depicted by Eq. (2.20).

$$\lim_{\lambda_r \to \infty} \frac{1}{1+\lambda_r^2} = 0 \tag{2.20}$$

Setting the right-hand side of Eq. (2.19) equal to 0 in order to find the zeroes, as done so in Eq. (2.21), reveals the upper bound for a.

$$\frac{1-3a}{-2(2a-1)^3} = 0 \tag{2.21}$$

As an overview, as λ_r tends to infinity, the value for a approaches $\frac{1}{3}$ with the exception that $a \neq \frac{1}{2}$.

2.1.2 Derivation of Maximum Power Coefficient

Knowing these optimum flow conditions based on Glauert's model can allow for the exact solution for C_P to be determined. Returning back to Eq. (2.2), there is the $\lambda_r^3 d\lambda_r$ term that must be accounted for in order to fully represent the integral for C_P as a function of a. An approach to this would be differentiating both sides of Eq. (2.9), which will result in a new expression for $2\lambda_r d\lambda_r$.

$$2\lambda_r d\lambda_r = \frac{6(4a-1)(1-2a)^2}{(1-3a)^2} da \tag{2.22}$$

The $\lambda_r^3 d\lambda_r$ term of interest can then be broken into a λ_r^2 and $\lambda_r d\lambda_r$ term, for which Equations 2.9 and 2.22 can be substituted in. Now, the integral for the maximum power coefficient can be defined by just one unknown, a, as done so in Eq. (2.23). Note that the limits of integration have been modified to account for the variable substitution from λ_r to a. The value of the lower bound, a_1, can be calculated by setting λ_r equal to 0 in Eq. (2.10) and solving for a such that $a_1 = \frac{1}{4}$. The upper bound, a_2 is the solution to Eq. (2.10) for a variable input of λ_r.

$$\begin{aligned} C_{Pmax} &= \frac{8}{\lambda^2} \int_0^{\lambda} a'(1-a)\lambda_r^2 \cdot \lambda_r \, d\lambda_r \\ &= \frac{24}{\lambda^2} \int_{a_1}^{a_2} \frac{(1-a)^2(1-4a)^2(1-2a)^2}{(1-3a)^2} da \end{aligned} \tag{2.23}$$

Through integration by substitution, a new variable $x = 1 - 3a$ is introduced to allow for ease of calculability. Differentiating this equation for x with respect to a allows for da to be rewritten as $-\frac{1}{3}dx$. From here, the exact integral can be expressed in terms of only x as shown by Eq. (2.24), and furthermore, it can be solved analytically. Note that the integration bounds must be adjusted to account for the substitution from a into terms of x.

$$C_{Pmax} = -\frac{1}{\lambda^2} \cdot \frac{8}{729} \int_{x_1}^{x_2} \left[\frac{(x+2)(4x-1)(2x+1)}{x} \right]^2 dx \tag{2.24}$$

An intermediate step simplifying the terms within the integral is shown in Eq. (2.25). To avoid representing the exact integral as a negative expression, the bounds of integration have been switched instead. Therefore, the lower limit becomes $x_2 = 1 - 3a_2$ and the upper limit becomes $x_1 = 1 - 3a_1 = \frac{1}{4}$.

$$C_{Pmax} = \frac{1}{\lambda^2} \cdot \left(\frac{2}{9}\right)^3 \int_{x_2}^{x_1} \left[64x^4 + 288x^3 + 372x^2 + 76x - 63 - \frac{12}{x} + \frac{4}{x^2} \right] dx \tag{2.25}$$

The exact solution for C_{Pmax} has been depicted in Eq. 2.26. Hence, we obtain:

$$C_{Pmax} = \frac{1}{\lambda^2} \cdot \left(\frac{2}{9}\right)^3 \left[\frac{64}{5}x^5 + 72x^4 + 124x^3 + 38x^2 - 63x - 12lnx - \frac{4}{x} \right]_{x_2 = 1-3a_2}^{x_1 = \frac{1}{4}} \tag{2.26}$$

The λ^2 term within the denominator of the C_{Pmax} exact solution is being evaluated at $\lambda^2 = \lambda_r^2|_{a_2}$; therefore, Eq. (2.9) can be substituted into the denominator as done so in Eq. (2.27). It is evident that at exactly $\lambda_r = 0$, where $a_2 = \frac{1}{4}$, there exists a singularity where C_{Pmax} is not defined. Therefore, a limit for C_{Pmax} as λ_r approaches 0, or as a_2 approaches $\frac{1}{4}$, must be taken as completed in Eq. (2.28). Below, C represents the constant value computed by evaluating the terms within the square brackets in Eq. (2.26) at x_1.

$$C_{Pmax} = \frac{(1-3a_2)}{(1-a_2)(1-4a_2)^2} \cdot \left(\frac{2}{9}\right)^3 \Bigg[C - \frac{64}{5}(1-3a_2)^5 + 72(1-3a_2)^4 + 124(1-3a_2)^3 + 38(1-3a_2)^2 - 63(1-3a_2) - 12ln(1-3a_2) - \frac{4}{(1-3a_2)}\Bigg] \tag{2.27}$$

$$\lim_{a_2 \to \frac{1}{4}} C_{Pmax} = \frac{0}{0} \tag{2.28}$$

Since evaluating this limit results in the indeterminate form of $\frac{0}{0}$, the mathematical theorem known as L'Hôpital's rule can be applied to determine the true limit using derivatives. The theorem equates the following limits, where c is a point on an open interval for which functions f and g are differentiable:

$$\lim_{a_2 \to c} \frac{f(a_2)}{g(a_2)} = \lim_{a_2 \to c} \frac{f'(a_2)}{g'(a_2)} = \lim_{a_2 \to c} \frac{f''(a_2)}{g''(a_2)} \tag{2.29}$$

For ease of reference, the functions f and g extracted from Eq. (2.27) have been explicitly stated below in Eqs. (3.12) and (3.13), respectively.

$$f(a_2) = \left(\frac{2}{9}\right)^3 \Bigg[C - \frac{64}{5}(1-3a_2)^5 + 72(1-3a_2)^4 + 124(1-3a_2)^3 + 38(1-3a_2)^2 - 63(1-3a_2) - 12ln(1-3a_2) - \frac{4}{(1-3a_2)}\Bigg] \tag{2.30}$$

$$g(a_2) = \frac{(1-a_2)(1-4a_2)^2}{1-3a_2} \tag{2.31}$$

$$\lim_{a_2 \to \frac{1}{4}} \frac{f'(a_2)}{g'(a_2)} = \lim_{a_2 \to \frac{1}{4}} \frac{\frac{24(64a_2^6 - 224a_2^5 + 308a_2^4 - 212a_2^3 + 77a_2^2 - 14a_2 + 1)}{(3a_2-1)^2}}{\frac{6(4a_2-1)(4a_2^2 - 4a_2 + 1)}{(3a_2-1)^2}} = \frac{0}{0} \tag{2.32}$$

Applying L'Hôpital's rule twice proves the following: $\lim_{a_2 \to \frac{1}{4}} C_{Pmax} = \frac{f''(a_2)}{g''(a_2)} = 0$. For explicitness, the limit of the ratio of $f''(a_2)$ and $g''(a_2)$ has been listed out in Eq. (2.33).

$$\lim_{a_2 \to \frac{1}{4}} \frac{f''(a_2)}{g''(a_2)} = \lim_{a_2 \to \frac{1}{4}} \frac{96(192a_2^6 - 600a_2^5 + 742a_2^4 - 467a_2^3 + 159a_2^2 - 28a_2 + 2)}{12(24a_2^3 - 24a_2^2 + 8a_2 - 1)} = 0 \tag{2.33}$$

These results for C_{Pmax}, representing Glauert's optimum model, have been plotted for a range of λ as seen in Fig. 2.2. The black dotted horizontal line represents the theoretical Betz limit at $\frac{16}{27} = 0.593$. The analytical solution derived from Glauert's optimum model approaches within 2% of the Betz limit at tip speed ratios greater than 7.5.

Table 2.2: Maximum power coefficient, C_{Pmax}, for Glauert's actuator disk model.

λ	C_{Pmax}
$\rightarrow 0$	0
1	0.415496
2	0.511187
3	0.545398
4	0.561487
5	0.570387
6	0.575859
7	0.579479
8	0.582007
9	0.583848
10	0.585234

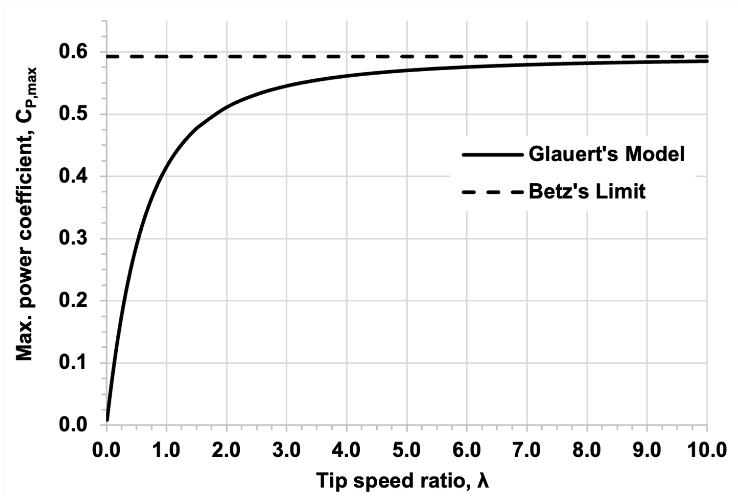

Figure 2.2: Maximum power coefficient, C_{Pmax}, for Glauert's actuator disk model and Betz's theoretical limit.

As shown above, this is the classical solution found by Glauert's original optimum rotor model. In later sections, some new transformations are developed to analytically determine exact solutions to both thrust coefficient, C_T, and bending moment coefficient, C_{Be}.

2.2 Optimum Wind Turbine Rotor Models in Literature

There exist various aerodynamic rotor models in literature that define optimum performance of a wind turbine using slightly different approximations. For the purpose of this thesis, Glauert's optimum model, which is widely accepted by the researchers in the wind energy discipline, has been explored in great detail. However, it is still imperative to understand alternate aerodynamic models, especially for the purpose of identifying existing models' limitations, as well as building on Glauert's accepted empirical approach.

The calculus detailing Glauert's theory has been shown in earlier sections, but essentially his assumption is as follows: streamtube elements behave separately from each other, so an annulus by annulus approach can be taken. Again, Glauert optimized $f(a,a') = a'(1-a)$ for each λ_r individually, which resulted in the '1st Relation' depicted by Eq. (1.15).

Another optimum rotor model was devised by Burton, Sharpe et al, where it was proposed that the additional pressure terms Glauert included in his analysis could be neglected—the only contributor to power extraction would then be the rate of change in axial momentum. This resulted in the following relation:

$$\lambda_r^2 = \frac{a(1-a)}{a'}. \tag{2.34}$$

Ultimately, it was concluded that the optimal turbine performance was at a constant axial induction factor and variable angular induction factor:

$$a = \frac{1}{3} \tag{2.35}$$

and

$$a' = \frac{2}{9\lambda_r^2}. \tag{2.36}$$

This model proved that regardless of tip speed ratio, the C_{Pmax} for an optimum rotor remained at $\frac{16}{27}$, which is the Betz limit.

The next optimum rotor model studied was of Joukowsky's, which was based on the assumption that a rotor is subject to constant circulation, where $\Gamma = 2\pi r u_\theta$; here, u_θ is the azimuthal velocity directly behind the rotor plane. Using this optimum model, the relations for axial and angular induction factors were as follows:

$$125a^5 - 325a^4 + 290a^3 - 106a^2 + (17 - 12\lambda^4)a + 4\lambda^2 - 1 = 0 \tag{2.37}$$

and

$$a' = \frac{\lambda^2}{\lambda_r^2} \cdot \frac{(3a-1)^{1/2}}{(5a-1)^{1/2}}. \tag{2.38}$$

This model is not applicable for tip speed ratios any less than 0.93. The C_{Pmax} values calculated using the Joukowsky model are always above the Betz limit of $\frac{16}{27}$, converging to this limit as the tip speed ratio tends to infinity.

The final optimum model that will be discussed is of Burton et al, which provided an approximation to Glauert's work. Burton's assumption was that the sole contributor to power extraction was the rate of change in axial momentum, and that additional pressure terms should be ignored. His altered '1st Relation' then became what is seen in Eq. (2.39) [14].

$$\lambda_r^2 = \frac{a(1-a)}{a'} \tag{2.39}$$

One can observe that the $(1 + a')$ term in the denominator of the original relation presented in Eq. (1.15) has been removed; this is based on the assumption that $(1 + a') \approx 1$ [10].

Chapter 3

Amendment to Glauert's Optimum Rotor Model

3.1 Derivation of Thrust Coefficient Based on Glauert's Optimum Solution

In wind turbine aerodynamics, the force of the wind on the rotor is known as thrust, which acts in the streamwise direction. Returning to actuator disk theory, the incremental thrust, dT produced by each annulus can be related to the pressure jump across the disk, as well as the area of the local disk annulus:

$$dT = \Delta p \, dA \tag{3.1}$$

Based on actuator disk theory, the pressure jump, Δp becomes: $\Delta p = 2\rho V_0^2 a(1-a)$. For a circular disk, dA is simply: $dA = 2\pi r dr$. As a result, the incremental thrust can be rewritten as shown in Eq. (3.2).

$$dT = 4\pi\rho V_0^2 a(1-a) r dr \tag{3.2}$$

Dividing these results by $\frac{1}{2}\rho A V_0^2$ yields a simplified expression for dC_T.

$$dC_T = \frac{8}{\lambda^2} a(1-a)\lambda_r d\lambda_r \tag{3.3}$$

Similar to how the exact integral for C_P was computed over a range of tip speed ratios, the integral for C_T can also be solved analytically using Glauert's optimum flow distributions. C_T is defined by the integral in Eq. (3.7), where integration by substitution is applied once again. The same substitution is carried through, where $x = 1 - 3a$. The exact solution for C_T has been depicted below.

$$\begin{aligned} C_T &= \frac{8}{\lambda^2}\int_0^{\lambda} a(1-a)\lambda_r \, d\lambda_r \\ &= -\frac{24}{\lambda^2}\int_0^{\lambda} \frac{a(1-a)(1-4a)(1-2a)^2}{(1-3a)^2} da \end{aligned} \tag{3.4}$$

$$C_T = \frac{1}{\lambda^2}\cdot\frac{8}{243}\int_{x_2}^{x_1}\left[\frac{(1-x)(2+x)(1-4x)(1+2x)^2}{x^2}\right]dx \tag{3.5}$$

$$C_T = -\frac{1}{\lambda^2}\cdot\frac{8}{243}\int_{x_1}^{x_2}\left(16x^3 + 28x^2 - 20x - 25 - \frac{1}{x} + \frac{2}{x^2}\right)dx \tag{3.6}$$

$$C_T = \frac{1}{\lambda^2}\cdot\frac{8}{243}\left[4x^4 + \frac{28}{3}x^3 - 10x^2 - 25x - ln x - \frac{2}{x}\right]_{x_2=1-3a_2}^{x_1=\frac{1}{4}} \tag{3.7}$$

To better understand the behavior of the C_T function, Eq. (3.7) is rewritten in terms of solely a. This can be done by substituting the '1st Relation' for λ_r^2 in the denominator above. Additionally, the values for x_1 and x_2 should be substituted in as well, being $\frac{1}{4}$ and $(1-3a_2)$ respectively, where a_2 is simply $a(\lambda_r)$.

$$\lambda^2 = \lambda_r^2|_{a_2} \tag{3.8}$$

$$\begin{aligned} C_T = \frac{(1-3a_2)}{(1-a_2)(1-4a_2)^2} \cdot \frac{8}{243} \Bigg[&\Big(4(\frac{1}{4})^4 + \frac{28}{3}(\frac{1}{4})^3 - 10(\frac{1}{4})^2 - 25(\frac{1}{4}) - ln(\frac{1}{4}) - 8 \Big) \\ - \Big(4(1-3a_2)^4 + \frac{28}{3}(1-3a_2)^3 &- 10(1-3a_2)^2 - 25(1-3a_2) - ln(1-3a_2) - \frac{2}{(1-3a_2)} \Big) \Bigg] \end{aligned} \tag{3.9}$$

At exactly $\lambda_r = 0$, where $a_2 = \frac{1}{4}$, there exists a singularity and C_T is not defined. Therefore, a limit for C_T as λ_r approaches 0, or as a_2 approaches $\frac{1}{4}$, must be taken as shown in Eq. (3.10).

$$\lim_{a_2 \to \frac{1}{4}} C_T = \frac{0}{0} \tag{3.10}$$

Since evaluating this limit results in the indeterminate form of $\frac{0}{0}$, the mathematical theorem known as L'Hôpital's rule can be applied to determine the true limit using derivatives. The theorem equates the following limits, where c is a point on an open interval for which functions f and g are differentiable:

$$\lim_{a_2 \to c} \frac{f(a_2)}{g(a_2)} = \lim_{a_2 \to c} \frac{f'(a_2)}{g'(a_2)} \tag{3.11}$$

For ease of reference, the functions f and g extracted from Eq. (3.9) have been explicitly stated below in Eqs. (3.12) and (3.13), respectively. Here, C represents the constant first term within the square brackets of Eq. (3.9).

$$\begin{aligned} f(a_2) = &\frac{8}{243} \Bigg[C - \Big(4(1-3a_2)^4 + \frac{28}{3}(1-3a_2)^3 - 10(1-3a_2)^2 \\ &- 25(1-3a_2) - ln(1-3a_2) - \frac{2}{(1-3a_2)} \Big) \Bigg] \end{aligned} \tag{3.12}$$

$$g(a_2) = \frac{(1-a_2)(1-4a_2)^2}{1-3a_2} \tag{3.13}$$

Applying L'Hôpital's rule once results in the following expressions for $f'(a_2)$ and $g'(a_2)$, shown by the limit of C_T as a_2 approaches $\frac{1}{4}$ in Eq. (3.14). Both functions have the $(3a_2-1)^2$ term appearing in the denominator, which can be cancelled out with one another. Again, the $\lim_{a_2 \to \frac{1}{4}} \frac{f'(a_2)}{g'(a_2)}$ results in the indeterminate form of $\frac{0}{0}$.

$$\lim_{a_2 \to \frac{1}{4}} \frac{f'(a_2)}{g'(a_2)} = \lim_{a_2 \to \frac{1}{4}} \frac{\dfrac{-24a_2(16a_2^4 - 36a_2^3 + 28a_2^2 - 9a_2 + 1)}{(3a_2-1)^2}}{\dfrac{6(4a_2-1)(4a_2^2 - 4a_2 + 1)}{(3a_2-1)^2}} = \frac{0}{0} \tag{3.14}$$

It is valid to apply L'Hôpital's rule a second time, as the indeterminate solution is retained. Equation (3.15) displays the $\lim_{a_2 \to \frac{1}{4}} \frac{f''(a_2)}{g''(a_2)}$, which does indeed result in a_2 definite value of 0.75.

$$\lim_{a_2 \to \frac{1}{4}} \frac{f''(a_2)}{g''(a_2)} = \lim_{a_2 \to \frac{1}{4}} \frac{-80a_2^4 + 144a_2^3 - 84a_2^2 + 18a_2 - 1}{12a_2^2 - 10a_2 + 2} = 0.75 \tag{3.15}$$

The behavior of the C_T function for λ_r ranging from 0 to 10 has been plotted in Fig. 3.1. As the tip speed ratio approaches 0, C_T converges to 0.75 as proven earlier. On the upper end of the λ_r range, the value of C_T approaches $\frac{8}{9}$. Recall back to actuator disk theory, where the definition is: $C_T = 4a(1-a)$. Note that at the upper limit of λ_r at $a = \frac{1}{3}$ also resulted in the same definite value of $\frac{8}{9}$.

Table 3.1: Thrust coefficient, C_T, for Glauert's actuator disk model.

λ	C_T
0.001	0.750192
1	0.845797
2	0.868902
3	0.877260
4	0.881210
5	0.883400
6	0.884749
7	0.885643
8	0.886267
9	0.886722
10	0.887065

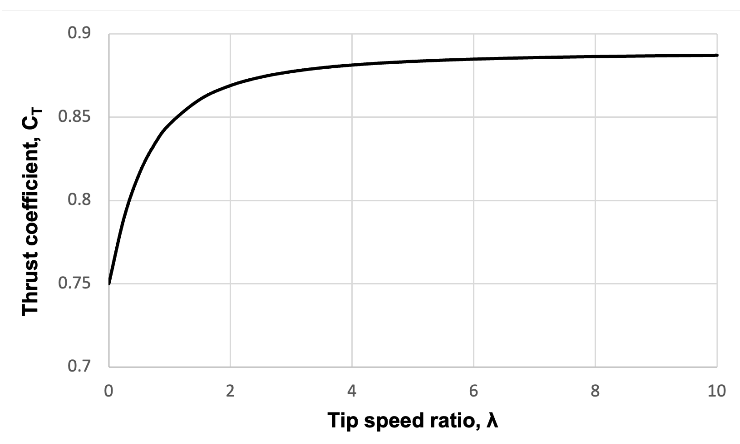

Figure 3.1: Thrust coefficient C_T as a function of tip speed ratio, λ. for optimal a and a' distribution.

3.2 Derivation of Bending Moment Coefficient Based on Glauert's Optimum Solution

The bending moment is an important structural parameter when assessing the loading of wind turbine blades, whether this be in the design phase or in fatigue studies. Equation (3.16) showcases the general definition of elemental bending moment, dBe, as well as its relation to the elemental thrust, dT and the local lever arm r.

$$dBe = dC_{Be} \cdot \frac{1}{2}\rho A V_0^2 R = dT \cdot r \tag{3.16}$$

Rewriting the equation for dC_{Be} in terms of dC_T allows for Eq. (3.3) to be substituted in, after which integration can take place in order to solve for C_{Be} exactly.

$$\begin{aligned} dC_{Be} &= dC_T \cdot \frac{r}{R} \\ &= \frac{8}{\lambda^2} a(1-a)\lambda_r d\lambda_r \cdot \frac{r}{R} \\ &= \frac{8}{\lambda^3} a(1-a)\lambda_r^2 d\lambda_r \end{aligned} \tag{3.17}$$

$$C_{Be} = \int dC_{Be} = \frac{8}{\lambda^3}\int_0^{\lambda} a(1-a)\lambda_r^2 d\lambda_r \tag{3.18}$$

The exact integral for the bending moment coefficient is defined by Eq. (3.18). Identical integration substitution is performed where $x = 1 - 3a$ so that C_{Be} can be solved for analytically, as shown in Eq. (3.19). Again, C_{Be} is defined using Glauert's optimum a and a' flow conditions.

$$\begin{aligned} C_{Be} &= \frac{8}{\lambda^3}\int_0^{\lambda} a(1-a)\lambda_r^2\, d\lambda_r \\ &= -\frac{24}{\lambda^3}\int_0^{\lambda} \frac{a(1-a)^{3/2}(1-4a)^2(1-2a)^2}{(1-3a)^{5/2}} da \end{aligned} \tag{3.19}$$

$$C_{Be} = \frac{1}{\lambda^3} \cdot \frac{8}{243 \cdot 27^{1/2}} \int_{x_1}^{x_2} \frac{(1-x)(2+x)^{3/2}(1-4x)^2(1+2x)^2}{x^{5/2}} dx \tag{3.20}$$

$$\begin{aligned} C_{Be} = \frac{1}{\lambda^3} \cdot \frac{8}{243 \cdot 27^{1/2}} \Bigg[&-24ln((x+2)^{1/2} + x^{1/2}) \\ &- \frac{(x+2)^{1/2}(192x^6 + 408x^5 - 532x^4 - 890x^3 + 585x^2 - 260x + 20)}{15x^{3/2}} \Bigg]_{x_2 = 1-3a_2}^{x_1 = \frac{1}{4}} \end{aligned} \tag{3.21}$$

To better understand the behavior of the C_{Be} function, Eq. (3.23) has been rewritten in terms of solely a. This means substituting Eq. (3.22) in for λ_r^3 in the denominator. The values for x_1 and x_2 should be substituted in as well, being $\frac{1}{4}$ and $(1 - 3a_2)$ respectively, where a_2 is simply $a(\lambda_r)$.

$$\lambda_r^3 = -\frac{(1-a_2)^{\frac{3}{2}}(1-4a_2)^3}{(1-3a_2)^{\frac{3}{2}}} \tag{3.22}$$

$$\begin{aligned} C_{Be} = &-\frac{(1-3a_2)^{3/2}}{(1-a_2)^{3/2}(1-4a_2)^3}\cdot\frac{8}{243\cdot 27^{1/2}}\Bigg[\Big(-24ln[(\frac{1}{4}+2)^{1/2}+(\frac{1}{4}]^{1/2})\\ &-\frac{(\frac{1}{4}+2)^{1/2}\cdot(192(\frac{1}{4})^6+408(\frac{1}{4})^5-532(\frac{1}{4})^4-890(\frac{1}{4})^3+585(\frac{1}{4})^2-260(\frac{1}{4})+20)}{15\cdot(\frac{1}{4})^{3/2}}\Big)\\ &-\Big(-24ln[(3-3a_2)^{1/2}+(1-3a_2)^{1/2}]\\ &-\frac{(3-3a_2)^{1/2}\cdot(192(1-3a_2)^6+408(1-3a_2)^5-532(1-3a_2)^4-890(1-3a_2)^3)}{15\cdot(1-3a_2)^{3/2}}\\ &+\frac{-585(1-3a_2)^2+260(1-3a_2)-20)}{15\cdot(1-3a_2)^{3/2}}\Big)\Bigg] \end{aligned} \tag{3.23}$$

$$\lim_{a\to\frac{1}{4}} C_{Be} = \frac{0}{0} \tag{3.24}$$

For ease of reference, the functions f and g extracted from Eq. (3.23) have been explicitly stated below in Eqs. (3.25) and (3.26) respectively. Here, C represents the constant first term within the square brackets of Eq. (3.23).

$$\begin{aligned} f(a) = &\frac{8}{243\cdot 27^{1/2}}\Bigg[C-\Big((-24ln[(3-3a_2)^{1/2}+(1-3a_2)^{1/2}]\\ &-\frac{(3-3a_2)^{1/2}\cdot(192(1-3a_2)^6+408(1-3a_2)^5-532(1-3a_2)^4-890(1-3a_2)^3)}{15\cdot(1-3a_2)^{3/2}}\\ &+\frac{-585(1-3a_2)^2+260(1-3a_2)-20)}{15\cdot(1-3a_2)^{3/2}}\Big)\Bigg] \end{aligned} \tag{3.25}$$

$$g(a) = -\frac{(1-a_2)^{3/2}(1-4a_2)^3}{(1-3a_2)^{3/2}} \tag{3.26}$$

Using L'Hôpital's rule as shown in Eq. (3.29) leads to the indeterminate form of $\frac{0}{0}$.

$$f'(a_2) = \frac{3359232a_2^7-11757312a_2^6+16166304a_2^5-11127456a_2^4+4041576a_2^3-734832a_2^2+52488a_2}{3^{\frac{13}{2}}\,(1-3a_2)^{\frac{5}{2}}\,(3-3a_2)^{1/2}} \tag{3.27}$$

$$g'(a_2) = \frac{9(1-a_2)^{1/2}\,(4a_2-1)^2\,(4a_2^2-4a_2+1)}{(1-3a_2)^{\frac{5}{2}}} \tag{3.28}$$

$$C_{Be} = \lim_{a_2 \to \frac{1}{4}} \frac{f'(a_2)}{g'(a_2)} \; = \frac{0}{0} \tag{3.29}$$

L'Hôpital's rule was applied twice more to evaluate the limit to a definite value, being 0.50 as displayed in Eq. (3.35).

$$f''(a_2) = \frac{\begin{array}{r}120932352a_2^8 - 519001344a_2^7 + 925888320a_2^6 - 893765664a_2^5 + 509553504a_2^4 \\ - 175414896a_2^3 + 35429400a_2^2 - 3779136a_2 + 157464\end{array}}{3^{\frac{13}{2}}\left(1-3a_2\right)^{\frac{7}{2}}\left(3-3a_2\right)^{3/2}} \tag{3.30}$$

$$g''(a_2) = \frac{3456a_2^5 - 7776a_2^4 + 6624a_2^3 - 2736a_2^2 + 558a_2 - 45}{(1-3a_2)^{7/2}(1-a_2)^{1/2}} \tag{3.31}$$

$$C_{Be} = \lim_{a_2 \to \frac{1}{4}} \frac{f''(a_2)}{g''(a_2)} \; = \frac{0}{0} \tag{3.32}$$

$$f'''(a_2) = \frac{\begin{array}{r}3265173504a_2^9 - 16597965312a_2^8 + 36147435840a_2^7 - 44231007744a_2^6 + 33530384160a_2^5 \\ - 16363658880a_2^4 + 5158048248a_2^3 - 1017532368a_2^2 + 114791256a_2 - 5668704\end{array}}{3^{\frac{13}{2}}\left(1-3a_2\right)^{\frac{9}{2}}\left(3-3a_2\right)^{\frac{5}{2}}} \tag{3.33}$$

$$g'''(a_2) = \frac{10368a_2^6 - 31104a_2^5 + 36288a_2^4 - 21312a_2^3 + 6642a_2^2 - 1026a_2 + 63}{\left(1-3a_2\right)^{\frac{9}{2}}\left(1-a_2\right)^{\frac{3}{2}}} \tag{3.34}$$

$$C_{Be} = \lim_{a_2 \to \frac{1}{4}} \frac{f'''(a_2)}{g'''(a_2)} \; = 0.50 \tag{3.35}$$

Table 3.2: Bending moment coefficient, C_{Be}, for Glauert's actuator disk model.

λ	C_{Be}
0.001	0.500144
1	0.568533
2	0.582845
3	0.587443
4	0.589431
5	0.590459
6	0.591058
7	0.591436
8	0.591691
9	0.591869
10	0.592000

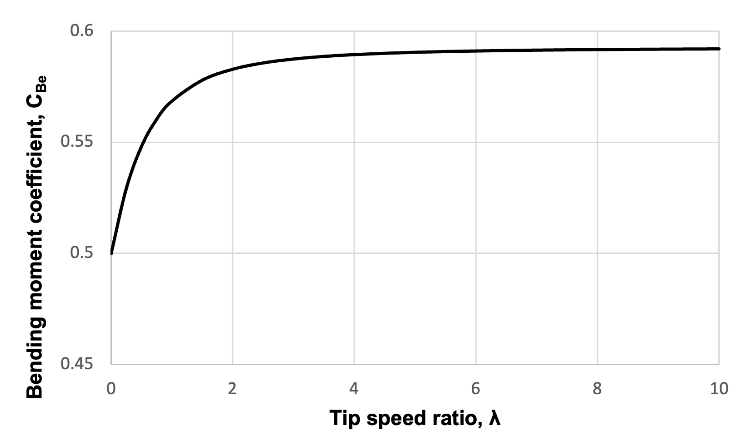

Figure 3.2: Bending moment coefficient C_{Be} as a function of tip speed ratio, λ. for optimal a and a' distribution.

3.3 Summary of Coefficients Derived from Glauert's Optimum Model

In Fig. 3.3, the three coefficients of interest, C_P, C_T, and C_{Be}, have been plotted over a range of design tip speed ratios from 0 to 10. As listed in the legend, C_P has been represented by a solid line, C_T by a dotted line, and C_{Be} by a dashed line. Note that Glauert's original work only showed the derivation of C_P based on optimum flow conditions. Exact analytical conditions to C_T and C_{Be} above constitute the first part of this work's amendment to Glauert's solution.

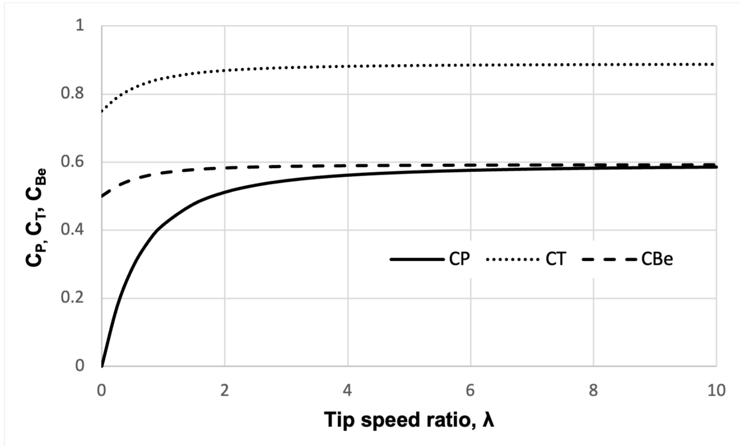

Figure 3.3: Power C_P, thrust C_T, and bending moment coefficients C_{Be} as functions of tip speed ratio, λ. for optimal a and a' distribution.

At $\lambda = 0$, there is zero C_P; however, there exists finite bending moment and thrust indicated by their respective coefficients, representing the loading of a non-rotating actuator disk. For this lower limit of λ, $C_{Be} = 0.5$ and $C_T = 0.75$. As depicted in the figure, C_P grows exponentially from 0 to 0.5852 over the observed interval for λ. C_T and C_{Be} do not follow similar growth trends as C_P; both coefficients increase at a fairly slower rate, with a percent increase of 18.25% and 18.37%, respectively. It is also interesting to note that the upper limit of both C_P and C_{Be} at $\lambda = 10$ hovers around approximately 0.59.

This visualization highlights the variation amongst the three coefficients of interest for increasing λ. For $\lambda > 6$, the coefficients all start to levelize approximately towards their upper limit; C_P shifts by 1.63%, however C_T's and C_{Be}'s variation remains under 0.5%.

For further visualization effects, the spanwise derivatives of power, thrust, and bending moment coefficients per unit length have been plotted along $\frac{r}{R}$ for the following λ's in Fig. 3.4: 2, 4, 6, 8, and 10. For added clarity, the exact definitions of the $\frac{dC_P}{d\frac{r}{R}}$, $\frac{dC_T}{d\frac{r}{R}}$, and $\frac{dC_{Be}}{d\frac{r}{R}}$ have been explicitly written out in Eqs. (3.36), (3.37), and (3.38).

$$\frac{dC_P}{d(\frac{r}{R})} = 8a'(1-a)\lambda_r^2 \cdot \frac{r}{R} \tag{3.36}$$

$$\frac{dC_T}{d(\frac{r}{R})} = 8a(1-a) \cdot \frac{r}{R} \tag{3.37}$$

$$\frac{dC_{Be}}{d(\frac{r}{R})} = 8a(1-a) \cdot (\frac{r}{R})^2 \tag{3.38}$$

Although the primary objective function in wind turbine optimization is to output maximum power, it is imperative to understand the relationship between various design parameters that C_P may influence. For instance, being cognizant of high root-flap bending moments and the resulting fatigue loads is also a note to be mindful of, since these require additional blade weight and cost

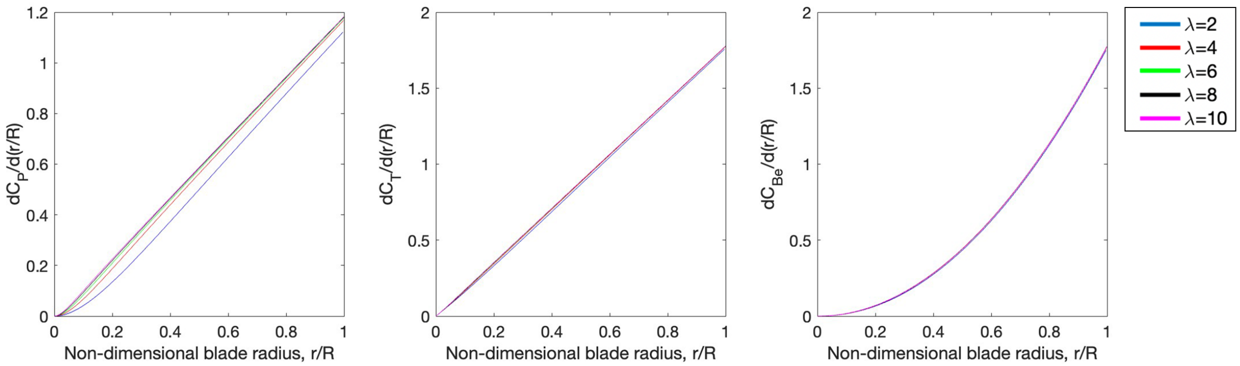

Figure 3.4: Spanwise derivatives of power, thrust, and bending moment coefficients per unit length as a function of the non-dimensional blade radius, $\frac{r}{R}$, for a range of design tip speed ratios.

[10]. Since the optimal C_P region corresponds to fairly constant C_{Be} values, minimizing the bending moment coefficient for maximum power coefficient is not a concern in this case.

3.4 A Calculus of Variations Approach to Glauert's Optimum Solution

As a review, Glauert's derivation of the optimum flow conditions has been presented in the first part of Section 2.1 of this thesis. An alternate mathematical approach to Glauert's method is taken to address the same optimization problem—maximizing C_P

3.4.1 Glauert's Optimum Rotor Model with Original Pressure Balance

Proceeding with an annulus-by-annulus approach, the mathematical method of Lagrange multipliers can be applied here under the constraint of a pressure jump, which the '1st Relation' from Eq. (1.15) accounts for. The Lagrangian function, as depicted in Eq. (3.39), relates the gradients of the function to the gradients of the set constraint, where $f(a, a')$ is the expression to be optimized for as defined in Eq. (3.40), Ω is the Lagrange multiplier, and $g(a, a')$ is the equality constraint of the '1st Relation' as defined in Eq. (3.41).

$$\mathcal{L}(a, a', \Omega) = f(a, a') + \Omega g(a, a') \tag{3.39}$$

$$f(a, a') = a'(1-a) \tag{3.40}$$

$$g(a, a') = a(1-a) - a'(1+a')\lambda_r^2 \tag{3.41}$$

To maximize $f(a, a')$ under the equality constraint of $g(a, a') = 0$, the stationary points of $\mathcal{L}(a, a', \Omega)$ must be determined by setting all partial derivatives of $\mathcal{L}$ with respect to a, a', and Ω equal to 0. Those partial derivatives become Eqs. (3.42), (3.43), and (3.44), respectively.

$$\frac{\partial \mathcal{L}}{\partial a} = -a' + \Omega(1-2a) = 0 \tag{3.42}$$

$$\frac{\partial \mathcal{L}}{\partial a'} = 1 - a - \Omega\lambda_r^2(1+2a') = 0 \tag{3.43}$$

$$\frac{\partial \mathcal{L}}{\partial \Omega} = a(1-a) - a'(1+a')\lambda_r^2 = 0 \tag{3.44}$$

3.4.2 Establishing a Relation for the Optimal Axial Induction Factor $a(\lambda_r)$

Starting with the first partial derivative, Eq. (3.42) can be rearranged to solve for $a'(\Omega, a)$, as shown:

$$a' = \Omega(1-2a) \tag{3.45}$$

This expression for a' is then to be substituted into the second partial derivative, Eq. (3.43). After some algebraic rearranging of the following Eq. (3.46), the quadratic formula can easily be applied in order to solve for $\Omega(a)$.

$$1 - a - \Omega\lambda_r^2[1 + 2\Omega(1-2a)] = 0 \tag{3.46}$$

$$\Omega^2(4a\lambda_r^2 - 2\lambda_r^2) + \Omega(-\lambda_r^2) + (1-a) = 0$$

$$\Omega = \frac{\lambda_r^2 \pm \sqrt{\lambda_r^4 - 4(4a\lambda_r^2 - 2\lambda_r^2)(1-a)}}{2(4a\lambda_r^2 - 2\lambda_r^2)}$$

The expression above for $\Omega(a)$ can then be substituted back into Eq. (3.45) to yield a simplified expression for $a'(a)$. Now, a' is solely a function of a:

$$a' = \frac{-\lambda_r^2 \pm \sqrt{\lambda_r^2 - 24a + 16a^2 + 8}}{4\lambda_r} \tag{3.47}$$

This simplified expression for $a'(a)$ is then substituted into the third partial derivative, Eq. (3.44), reducing to Eq. (3.48) for a which only varies based on the independent variable, λ_r.

$$a - a^2 - \frac{-\lambda_r^2 + 8a^2 - 12a + \lambda_r\sqrt{\lambda_r^2 + 16a^2 - 24a + 8} + 4}{8} = 0 \tag{3.48}$$

Upon further simplification, a fourth-order polynomial for for $a(\lambda_r)$ can be extracted as indicated by Eq. (3.49).

$$16a^4 - 40a^3 + (33 - 3\lambda_r^2)a^2 + (4\lambda_r^2 - 10)a + (1 - \lambda_r^2) = 0 \tag{3.49}$$

As referenced earlier in Eq. (2.10), Glauert's universal relation is of the third-order in comparison to the fourth-order polynomial from Eq. (3.49). Dividing Eq. (3.49) by its factor $a - 1$ recovers the original Glauert's polynomial from Eq. (2.10).

3.4.3 Establishing a Relation for the Optimal Angular Induction Factor $a'(\lambda_r)$

The same system of equations can be solved to compute a polynomial for $a'(\lambda_r)$. This time, Eq. (3.42) is solved for Ω rather than a', yielding the following:

$$\Omega = \frac{a'}{1-2a} \tag{3.50}$$

The steps used to solve for $a(a')$ from the second partial derivative, Eq. (3.43), can be observed below. Some algebraic rearranging has been performed so that the quadratic formula can simply be applied to solve for a.

$$1 - a - \frac{a'}{1-2a} \cdot \lambda_r^2(1+2a') = 0 \tag{3.51}$$

$$2a^2 - 3a + (1 - \lambda_r^2 a' - 2(a')^2\lambda_r^2) = 0$$

$$a = \frac{3 \pm \sqrt{9 - 8(1 - \lambda_r^2 a' - 2(a')^2\lambda_r^2)}}{4}$$

Finally, this solved expression for $a(a')$ is substituted into the third Lagrangian partial derivative, being Eq. (3.44). By doing as such, a polynomial for $a'(\lambda_r)$ can be extracted. An intermediate step has been shown in Eq. (3.52) before displaying the final third-order polynomial derived using this Lagrangian multiplier approach.

$$\frac{-\sqrt{1 + 8a'\lambda_r^2 + 16(a')^2\lambda_r^2} - 4a'\lambda_r^2 - 8(a')^2\lambda_r^2 + 1}{8} - a'(1+a')\lambda_r^2 = 0 \tag{3.52}$$

$$16\lambda_r^2(a')^3 + 24\lambda_r^2(a')^2 + (9\lambda_r^2 - 3)a' - 2 = 0 \tag{3.53}$$

Similar to Eq. (3.49), the relation for $a'(\lambda_r)$ presented in Eq. (3.53) also recovers Glauert's results.

3.5 Optimum Rotor Model of Burton, Sharpe et al. Using Modified Pressure Balance

The function $f(a, a')$ can be modified slightly to optimize for the complete expression within the C_P integral originally presented in Eq. (2.2), such that $f(a, a') = a'(1-a)\lambda_r^3$ now. Recall Glauert's approach, where the function to be optimized was truncated to $a'(1-a)$. This modification was observed within the work of Burton, Sharpe et al., where the assumption $1 + a' \approx 1$ was made, producing a new relation for λ_r^2 as previously shown in Eq. (2.34) [15].

Regardless, the same process from earlier is carried out to find the stationary points of $\mathcal{L}(a, a', \Omega)$. The partial derivatives now work out to be Eqs. (3.54), (3.55), and (3.56) respectively.

$$\frac{\partial \mathcal{L}}{\partial a} = -a'\lambda_r^3 + \Omega(1-2a) = 0 \tag{3.54}$$

$$\frac{\partial \mathcal{L}}{\partial a'} = \lambda_r^3(1-a) - \Omega(1+a')\lambda_r^2 = 0 \tag{3.55}$$

$$\frac{\partial \mathcal{L}}{\partial \Omega} = a(1-a) - a'(1+a')\lambda_r^2 = 0 \tag{3.56}$$

3.5.1 Modified Relation for Optimal Axial Induction Factor $a(\lambda_r)$

In order to solve this system of equations, the Lagrangian partial derivative with respect to a' will be addressed first. Equation (3.55) is solved for Ω.

$$\Omega = \frac{\lambda_r(1-a)}{1+a'} \tag{3.57}$$

The expression for Ω is then substituted back into the Lagrangian partial derivative with respect to a in Eq. (3.54), yielding the following:

$$-a'\lambda_r^3 + \frac{\lambda_r(1-a)}{1+a'}(1-2a) = 0$$

Once again, the equation is to be rearranged such that the quadratic formula can easily be applied in order to extract a polynomial for $a'(a)$.

$$\lambda_r^3(a')^2 + \lambda_r^3 a' - (1-a)(1-2a)\lambda_r = 0 \tag{3.58}$$

$$a' = \frac{-\lambda_r^3 \pm \sqrt{\lambda_r^6 + 4\lambda_r^4(1-a)(1-2a)}}{2\lambda_r^3} \tag{3.59}$$

This expression for a' is substituted into Eq. (3.56), which simplifies greatly into a quadratic equation for a solely dependent on the independent variable, λ_r. Upon solving Eq. (3.60), two solutions for a are determined.

$$a - a^2 - (2a-1)(a-1) = 0 \tag{3.60}$$

$$a = \frac{1}{3}, 1$$

Given that momentum theory is only valid for $a \subset (0, \frac{1}{2})$, the solution $a = 1$ can be eliminated, leaving $a = \frac{1}{3}$.

3.5.2 Modified Relation for Optimal Angular Induction Factor $a'(\lambda_r)$

Once again, the system of equations from 3.54 through 3.56 need to be solved to determine a polynomial for $a'(\lambda_r)$. Ω was also solved first with this approach, however the Lagrangian partial derivative with respect to a was used instead.

$$\Omega = \frac{a'\lambda_r^3}{1-2a} \tag{3.61}$$

Now, the expression for Ω can be substituted into Eq. (3.55) and simplified fully to obtain an expression for $a(a')$.

$$\lambda_r^3(1-a) - \frac{a'\lambda_r^3}{1-2a}(1+a')\lambda_r^2 = 0 \tag{3.62}$$

$$2\lambda_r^3 a^2 - 3\lambda_r^3 a + \lambda_r^3 - a'\lambda_r^3(1+a')\lambda_r^2 = 0$$

$$a = \frac{3+\sqrt{8\lambda_r^2(a')^2 + 8\lambda_r^2 a' + 1}}{4}$$

Thus, this expression is used in the final Lagrangian partial derivative with respect to Ω in order to eliminate the last unknown variable a. For simplicity, only one intermediate step and the final polynomial for the optimal axial induction factor using the complete term have been displayed.

$$\frac{-\sqrt{8\lambda_r^2(a')^2 + 8\lambda_r^2 a' + 1} - 4\lambda_r^2(a')^2 - 4\lambda_r^2 a' + 1}{8} - a'\lambda_r^2 - \lambda_r^2(a')^2 = 0 \tag{3.63}$$

$$9\lambda_r^2(a')^3 + 18\lambda_r^2(a')^2 + (9\lambda_r^2 - 2)a' - 2 = 0 \tag{3.64}$$

Interestingly, $(a'+1)$ is a factor of the polynomial in Eq. (3.64). Dividing this factor by this polynomial results in the second-order polynomial presented in Eq. (3.65).

$$9\lambda_r^2(a')^2 + 9\lambda_r^2 a' - 2 = 0 \tag{3.65}$$

Rewriting the equation above as an expression for a' yields the following relation presented in Eq. (3.66). As expected, this solution exactly matches the equality constraint set based on the '1st Relation' in Eq. (1.15), when computed at the optimum solution, $a = \frac{1}{3}$.

$$a' = -\frac{1}{2} + \frac{\sqrt{9\lambda_r^2 + 8}}{6\lambda_r} \tag{3.66}$$

3.6 Visual Representation of Flow Conditions Using Different Optimum Models

The iterative Newton–Raphson method was used to plot a and a' distributions based on the respective optimum relations. To the left, Fig. 3.5 highlights the variation present between Glauert's optimum rotor disk solution, the flow conditions derived in this section using the amended model, as well as the optimum rotor model of Burton and Sharpe. The $x-$ axis has been limited to a maximum of $\lambda_r = 6$, because variation amongst the two models beyond that chosen λ_r is negligible. To the right, the scaled spanwise distributions for $\lambda = 4$ (black) and $\lambda = 8$ (red) have been displayed representing the three models as well.

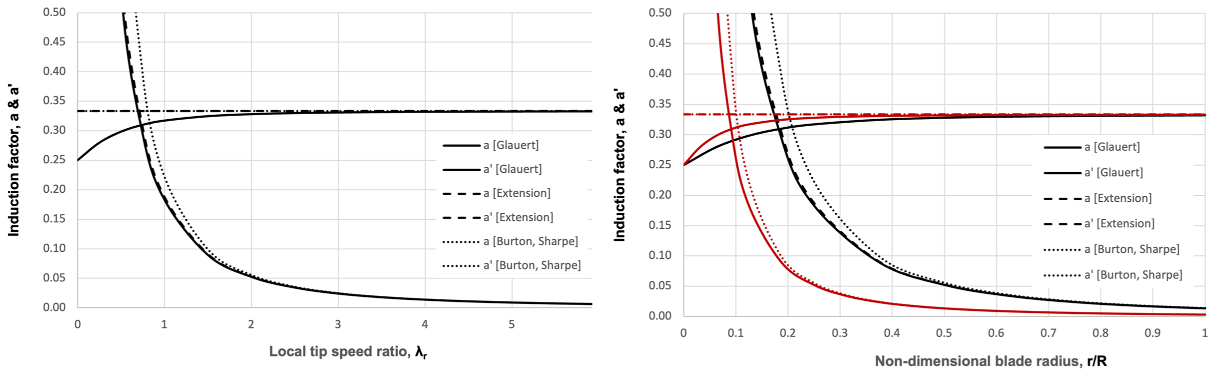

Figure 3.5: Comparison of optimum flow distributions for Glauert's solution, the amendment, and the optimum model of Burton and Sharpe using universal solution (left) and scaled spanwise distributions (right) for $\lambda = 4$ (black) and $\lambda = 8$ (red).

Glauert's optimum flow conditions have been noted by a solid line, whereas the optimum flow conditions based on the extended objective function have been displayed by a dashed line. The optimum rotor model of Burton and Sharpe has been displayed by the dotted line. Recall that the a distribution approaches $\frac{1}{3}$, whereas the a' distribution approaches 0 for increasing λ_r values. There exist minuscule differences between the three optimization models for desirable operating λ ranges.

To better understand how the variation in optimal a and a' distributions influence the maximum power coefficient, both the original and amended model's C_{Pmax} derived values have been displayed in Table 3.3, along with the associated percent errors. These same results have been plotted in Fig. 3.6

Table 3.3: Variation in maximum power coefficient between Glauert's actuator disk model ($C_{Pmax,G}$) and the amended model ($C_{Pmax,A}$).

λ_r	$C_{Pmax,G}$	$C_{Pmax,A}$	% Error
0.001	0.0009	0.5926	∞
1	0.4155	0.5926	42.62
2	0.5112	0.5926	15.92
3	0.5454	0.5926	8.65
4	0.5615	0.5926	5.54
5	0.5704	0.5926	3.89
6	0.5759	0.5926	2.91
7	0.5795	0.5926	2.26
8	0.5820	0.5926	1.82
9	0.5838	0.5926	1.50
10	0.5852	0.5926	1.26

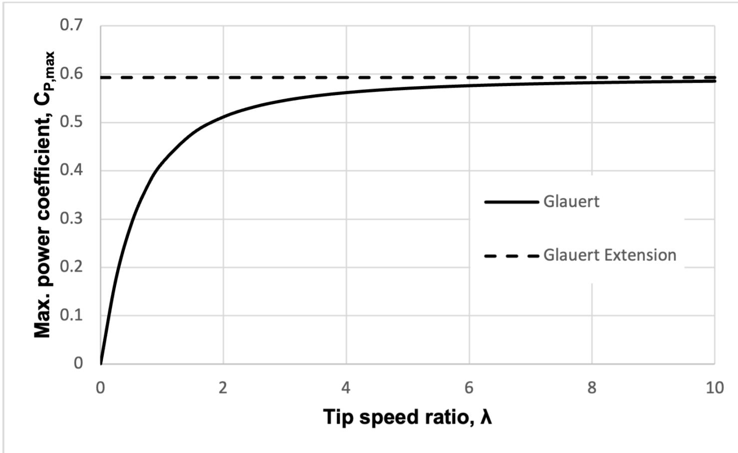

Figure 3.6: Power coefficient C_P variation between Glauert's model and the amended model for local tip speed ratios, λ_r.

Since the optimum a populated from the amended model was not a distribution, but rather a constant $\frac{1}{3}$, the associated C_{Pmax} value is also constant at 0.5926. Note that this value is very close to Betz's Limit of $\frac{16}{27}$, and Glauert's model approaches a slightly smaller value of C_{Pmax}, but nevertheless also approaches this limit. Figure 3.6 helps highlight the fact that the variation between the two models observed above is primarily prevalent for low λ, particularly under 5.

Using the same two models, being Glauert's and the amendment, the variation within C_T and C_{Be} can also be analyzed through Table 3.4 and 3.5, as well as Figs. 3.7 and 3.8.

Table 3.4: Variation in thrust coefficient, C_T, between Glauert's actuator disk model and the amended model.

λ_r	$C_{T,G}$	$C_{T,L}$	% Error
0.001	0.7502	0.8889	18.49
1	0.8458	0.8889	5.09
2	0.8689	0.8889	2.30
3	0.8773	0.8889	1.33
4	0.8812	0.8889	0.87
5	0.8834	0.8889	0.62
6	0.8847	0.8889	0.47
7	0.8856	0.8889	0.37
8	0.8863	0.8889	0.30
9	0.8867	0.8889	0.24
10	0.8871	0.8889	0.21

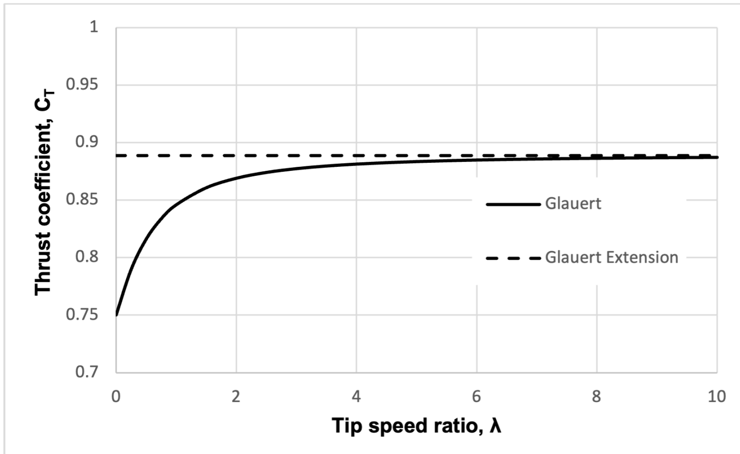

Figure 3.7: Thrust coefficient C_T variation between Glauert's model and the amended model for low tip speed ratios, λ_r.

Table 3.5: Variation in bending moment coefficient, C_{Be}, between Glauert's actuator disk model and the amended model.

λ_r	$C_{Be,G}$	$C_{Be,L}$	% Error
0.001	0.5001	0.5926	18.48
1	0.5685	0.5926	4.23
2	0.5828	0.5926	1.67
3	0.5874	0.5926	0.88
4	0.5894	0.5926	0.54
5	0.5905	0.5926	0.36
6	0.5911	0.5926	0.26
7	0.5914	0.5926	0.20
8	0.5917	0.5926	0.15
9	0.5919	0.5926	0.12
10	0.5920	0.5926	0.10

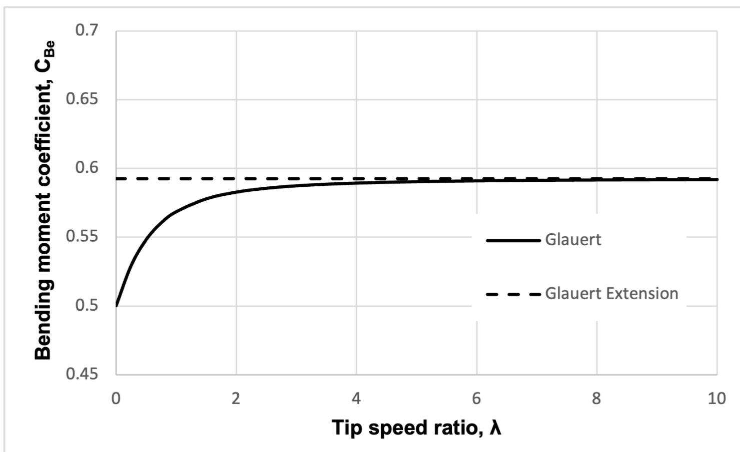

Figure 3.8: Bending moment coefficient C_{Be} variation between Glauert's model and the amended model for low tip speed ratios, λ_r.

Chapter 4

Conclusion and Future Work

4.1 Conclusion

Within this work, Glauert's optimum rotor disk solution was used to derive exact solutions for the power, thrust, and bending moment coefficients (C_P, C_T, and C_{Be}). L'Hôpital's theorem was employed to determine the convergence behavior of these coefficients as the tip speed ratio, λ, approached 0. It was determined that the limiting case for C_P, C_T, and C_{Be} was 0, 0.75, and 0.50 respectively. Additionally, an alternative approach using calculus of variations was taken to address the classical objective function in wind turbine optimization—to maximize C_P. The resulting optimum flow conditions recovered Glauert's optimum rotor solution, thus confirming the validity of this existing aerodynamic performance model using an alternate mathematical method. Next, the classical objective function is modified to study effects on optimum a and a' flow distributions, serving as an amendment to Glauert's optimization work. It is determined that for desired operating tip speed ratios ($\lambda > 4$), there is no considerable difference in optimum flow conditions between the amended model, Burton and Sharpe's work, and finally, Glauert's solution.

4.2 Future Work

Next steps include evolving the optimization problem to include a thrust constraint. In other words, how can one maximize the power coefficient, C_P, while holding the thrust coefficient, C_T, constant. With new turbine concepts such as the ”Low Induction Rotor,” where the rotor thrust and power is slightly compromised in order to decrease blade loading, it becomes of greater interest to understand how the optimum induction factors are affected. By implementing an equality constraint on C_T, one can better understand the optimal design space that considers root-flap bending moments, while also aiming for maximum power extraction by the wind turbine.

Bibliography

[1] N. Troldborg V. L. Okulov W. Z. Shen J. N. Sørensen, R. Mikkelsen. The aerodynamics of wind turbines. In James P. Denier and Matthew D. Finn, editors, *Mechanics Down Under*, pages 169–360. Springer Dordrecht, Netherlands, 2013.

[2] Marcelo Molina and Pedro Mercado. *Modelling and Control Design of Pitch-Controlled Variable Speed Wind Turbines*, pages 375–376. 04 2011.

[3] Wind power facts. https://cleanpower.org/facts/wind-power/. Accessed: 2024-01-24.

[4] H. Lee Core Writing Team and J. Romero (eds.). Climate change 2023: Synthesis report. contribution of working groups i, ii and iii to the sixth assessment report of the intergovernmental panel on climate change. *IPCC*, pages 35–115, 2023.

[5] Transforming our world: the 2030 agenda for sustainable development. https://sdgs.un.org/2030agenda, 2015. Accessed 24 January 2024.

[6] Brandon N. Owens. *The Wind Power Story*. John Wiley Sons, 2019.

[7] et al. Tony Burton. *Wind Energy Handbook*. John Wiley Sons, 2001.

[8] Wind turbines: the bigger, the better. https://www.energy.gov/eere/articles/wind-turbines-bigger-better. Accessed: 2024-03-25.

[9] Experts anticipate larger turbines and plants, with increasing focus on grid-value enhancement options. https://emp.lbl.gov/news/experts-anticipate-larger-turbines. Accessed: 2024-03-25.

[10] Sven Schmitz. *Aerodynamics of Wind Turbines: A Physical Basis for Analysis and Design*. John Wiley Sons, 2019.

[11] Jeremy Ledoux, Sebastián Riffo, and Julien Salomon. Analysis of the blade element momentum theory. *SIAM Journal on Applied Mathematics*, 81(6):2596–2621, 2021.

[12] Valery L. Okulov and Gijs A. M. van Kuik. The betz-joukowsky limit: on the contribution to rotor aerodynamics by the british, german and russian scientific schools. *Wind Energy*, 15(2):203–347, 2012.

[13] Hermann Glauert. Airplane propellers. In William Durand, editor, *Aerodynamic Theory*, pages 169–360. Springer, Berlin, Heidelberg, Farnborough, England, 1935.

[14] Jens Nørkær Sørensen. *General Momentum Theory for Horizontal Axis Wind Turbines*, chapter 4-5. Springer International Publishing, Switzerland, 4 edition, 2016.

[15] Sharpe D. Jenkins N. Burton, T. and E Bossanyi. *Wind Energy Handbook*. Wiley, 2002.